INTERNATIONAL JOURNAL FOR NUMERICAL METHODS IN FLUIDS, VOL. 9, 1025–1050 (1989)

ANALYSIS OF INCOMPRESSIBLE MASSIVELY SEPARATED VISCOUS FLOWS USING UNSTEADY NAVIER–STOKES EQUATIONS

K. N. GHIA, G. A. OSSWALD AND U. GHIA*

*Department of Aerospace Engineering and Engineering Mechanics, *Department of Mechanical and Industrial Engineering,*
University of Cincinnati, Cincinnati, OH 45221, U.S.A.

SUMMARY

The unsteady incompressible Navier–Stokes equations are formulated in terms of vorticity and streamfunction in generalized curvilinear orthogonal co-ordinates to facilitate analysis of flow configurations with general geometries. The numerical method developed solves the conservative form of the vorticity transport equation using the alternating direction implicit method, whereas the streamfunction equation is solved by direct block Gaussian elimination. The method is applied to a model problem of flow over a backstep in a doubly infinite channel, using clustered conformal co-ordinates. One-dimensional stretching functions, dependent on the Reynolds number and the asymptotic behaviour of the flow, are used to provide suitable grid distribution in the separation and reattachment regions, as well as in the inflow and outflow regions. The optimum grid distribution selected attempts to honour the multiple length scales of the separated flow model problem. The asymptotic behaviour of the finite differenced transport equation near infinity is examined and the numerical method is carefully developed so as to lead to spatially second-order-accurate wiggle-free solutions, i.e. with minimum dispersive error. Results have been obtained in the entire laminar range for the backstep channel and are in good agreement with the available experimental data for this flow problem, prior to the onset of three-dimensionality in the experiment.

KEY WORDS Unsteady Navier–Stokes equations Direct solution method Block Gaussian elimination Backstep channel Incompressible separated flow

1. INTRODUCTION

The accurate simulation of moderately high-Reynolds-number viscous flows in and around complex internal configurations of importance in turbomachinery applications is a formidable task. The flow fields for these complex configurations may involve any or all of the following features: unsteadiness, three-dimensionality, geometrical complexities, streamwise separation, recirculation, compressibility, turbulence, etc. For accurate prediction of aerodynamic losses and heat transfer rates in such configurations, it is important that the viscous flow field be predicted correctly. The present study is directed towards accurate simulation of viscous flows involving streamwise separation and unsteadiness, in addition to other features that may be present in the flow.

For viscous flows in configurations of practical interest, the Reynolds number is generally quite high. Nevertheless, the classical boundary layer theory is inadequate for prediction of such flows as they contain regions of separated flow, massive blowing, etc., where the boundary layer is sufficiently displaced from the body surface so as to alter the inviscid pressure distribution significantly. For this class of problems, where a significant displacement effect prevails, two viable approaches are available for predicting the viscous flow fields: (i) the first method is based

0271–2091/89/081025–26$13.00

Received 8 December 1987
Revised 25 July 1988

on an inviscid–viscous strong interaction analysis utilizing localized flow regions, whereas (ii) the second method consists of using, in the entire region of interest, a single set of equations which have the necessary mutual dependence between the inviscid and viscous flows built into them. Davis and Werle[1] have reviewed the progress of the strong interaction analysis, which is useful in describing a large class of boundary layer departure flows. The theoretical basis for the various strong interaction models lies in multistructured asymptotic analyses.[2–6] In these analyses the subscale flow structure embedded under the boundary-layer-like region is considered rigorously and the strong interaction approach is formally shown to provide an exact representation of the flow for asymptotically large Reynolds numbers. In the flow field of interest, as the displacement–interaction effects become significant, the 'triple-deck' theory aids in establishing the relative orders of the length scales required for the adjustment of a classical boundary layer as it enters a region of strong interaction and separation. However, for complex internal flows at finite Reynolds number, the prevailing flow may differ significantly from the predictions of the strong interaction model.

The second class of methods used in obtaining solutions for internal flows, in which viscous phenomena considerably alter the inviscid pressure field, is based on fully viscous analyses. In these analyses a single set of equations, valid in the entire flow field, is used, thus avoiding the need for dividing the flow field into inviscid and viscous regions. Of the three prominent approaches available in this category, two are based on reduced forms of the Navier–Stokes equations, whereas the third uses the complete Navier–Stokes equations. In the first approach the time-dependent thin-shear-layer equations are used[7] to successfully compute separated flows; this approach has been widely used. Rubin and co-workers have also calculated separated flows using the steady thin-layer form of the Navier–Stokes equations with the streamwise pressure gradient term represented by a forward difference approximation. The results obtained using this approach have been summarized by Rubin.[8] In the second approach the complete pressure interaction is included by using a Poisson equation for pressure, in lieu of the continuity equation. This has been termed a semi-elliptic formulation by Ghia *et al.*[9] who employed it to successfully compute separated flow inside a doubly infinite channel with an asymmetric constriction, using primitive variables. Ghia and Ghia[10] have proposed yet another semi-elliptic formulation for compressible viscous flow, which efficiently computes separated flow. Finally, separated internal flows are calculated using the complete Navier–Stokes equations by many researchers (see e.g. References 11–14). With this last approach it is possible to compute flows with large separated regions, where shear layers are not necessarily aligned with any one of the co-ordinates. Moreover, since the solution of the complete Navier–Stokes equations is generally based on the time-dependent equations, both unsteady as well as steady solutions can be determined numerically by explicit or implicit methods.

In general, implicit numerical methods display improved stability characteristics as compared to explicit methods, at the expense of increased arithmetic operations count. Therefore an implicit method for the solution of algebraic equations is recommended whenever the step size limitation imposed by the stability requirement for an explicit method is significantly less than the step size limitation imposed by the time scale resolution of the physical problem. Furthermore, the presence of multiple scales in a separated flow contributes to increased stiffness of the non-linear system of discretized algebraic equations and may also suggest the use of implicit solution techniques. Osswald and Ghia[14] have developed a direct method for the solution of two-dimensional, unsteady, incompressible Navier–Stokes equations in generalized orthogonal co-ordinates. This unsteady analysis was formulated using the derived variables, namely, vorticity ω and streamfunction ψ. In this method the streamfunction equation was solved using a block Gaussian elimination (BGE) technique. This direct Dirichlet Poisson solver in generalized orthogonal co-ordinates is very accurate and efficient, with computational gains of an order of magnitude over the corresponding iterative schemes. In a recent review of fast solvers for elliptic equations, Stüben[15] has shown that the Dirichlet Poisson problem with a 256 × 256 grid in Cartesian co-ordinates required one to two orders of magnitude higher computing time when solved by iterative schemes such as the alternating direction implicit (ADI) method and the successive over-relaxation (SOR) method, respectively, as compared to the time required by a direct solver such as that of Buneman. The efficiency and accuracy of the fast solvers make them very well suited for the solution of the Poisson equation in the unsteady analysis of flows using the complete Navier–Stokes equations.

The primary objective of the present study is to provide an accurate and efficient direct method for the solution of two-dimensional unsteady incompressible Navier–Stokes equations using orthogonal curvilinear co-ordinates. To achieve this goal, it was decided to refine the method developed by Osswald and Ghia[14] by incorporating in it the following improvements which could lead to a more realistic simulation of physical problems and increase the accuracy and efficiency of the overall solutions:

(i) For a class of internal flow configurations, with the length in the streamwise direction very large compared to the length in the normal direction, an estimate is made of all the local scales of the flow problems in order to provide a clustered grid distribution which honours these individual scales.

(ii) With the aid of an estimate of the asymptotic metric coefficients, a reduced form of the governing equations is obtained near infinity and the numerical solutions of these equations are used to provide consistent inflow and outflow boundary conditions.

(iii) The separated flow model problem selected is one for which laser–Doppler anemometer experimental data are available, so that the results obtained using the present analysis can be meaningfully assessed by comparison with these data.

2. GOVERNING EQUATIONS IN GENERALIZED ORTHOGONAL CO-ORDINATES

A considerable number of numerical simulations of 2D, laminar incompressible viscous flows have been obtained using the vorticity–streamfunction (ω, ψ) system. There are definite advantages in using this system as compared to the primitive variable (u, v, p) system. In this study it has been preferred to employ the (ω, ψ) system. The form of the governing differential equations and the notation used parallel those of Osswald and Ghia.[14] The conservation form of the two-dimensional, unsteady, incompressible Navier–Stokes equations, in terms of the vorticity ω and the streamfunction ψ, consist of a temporally parabolic, spatially elliptic vorticity transport equation

$$\frac{\partial \omega}{\partial t} + \nabla \cdot (\omega \mathbf{V}) = \frac{1}{Re} \nabla^2 \omega, \tag{1}$$

together with an elliptic Poisson equation for the streamfunction

$$\nabla^2 \psi = -\omega. \tag{2}$$

Here Re is the Reynolds number of the flow and the streamfunction is defined through the relation

$$\mathbf{V} = \nabla \psi \times \mathbf{k} \tag{3}$$

where $\mathbf{k}$ is the unit vector normal to the plane of the flow and $\mathbf{V}$ is the total velocity vector. A general orthogonal curvilinear co-ordinate system (ξ^1, ξ^2) is used in this study to provide nonuniform surface-oriented co-ordinates for arbitrary geometries. The new (ξ^1, ξ^2) co-ordinates can be related to the inertial Cartesian co-ordinate system (x^1, x^2) by an admissible co-ordinate transformation $\xi^i(x^1, x^2) \leftrightarrow x^j(\xi^1, \xi^2)$, $i, j = 1, 2$. In this co-ordinate system equations (1) and (2) take the following form:

$$\sqrt{g}\frac{\partial \omega}{\partial t} + \frac{\partial}{\partial \xi^1}\left(\omega \frac{\partial \psi}{\partial \xi^2}\right) - \frac{\partial}{\partial \xi^2}\left(\omega \frac{\partial \psi}{\partial \xi^1}\right) = \frac{1}{Re}\left[\frac{\partial}{\partial \xi^1}\left(\frac{g_{22}}{\sqrt{g}}\frac{\partial \omega}{\partial \xi^1}\right) + \frac{\partial}{\partial \xi^2}\left(\frac{g_{11}}{\sqrt{g}}\frac{\partial \omega}{\partial \xi^2}\right)\right] \tag{4}$$

and

$$\frac{\partial}{\partial \xi^1}\left(\frac{g_{22}}{\sqrt{g}}\frac{\partial \psi}{\partial \xi^1}\right) + \frac{\partial}{\partial \xi^2}\left(\frac{g_{11}}{\sqrt{g}}\frac{\partial \psi}{\partial \xi^2}\right) = -\sqrt{g}\,\omega. \tag{5}$$

Here g_{ij} are the elements of the covariant metric tensor and are defined as

$$g_{ij} = \sum_{k=1}^{2}\left(\frac{\partial x^k}{\partial \xi^i}\right)\left(\frac{\partial x^k}{\partial \xi^j}\right), \tag{6a}$$

and g is the determinant of the metric tensor. Since the (ξ^1, ξ^2) co-ordinate system is assumed orthogonal in the present study,

$$g_{12} = g_{21} = 0 \quad \text{(orthogonality condition)},$$

so that

$$g = g_{11}g_{22} \tag{6b}$$

and

$$\frac{g_{11}}{\sqrt{g}}\frac{g_{22}}{\sqrt{g}} = 1. \tag{6c}$$

For a general orthogonal co-ordinate transformation the metric coefficients $\sqrt{g}$, $g_{11}/\sqrt{g}$ and $g_{22}/\sqrt{g}$ will be functions of both ξ^1 and ξ^2, so that equations (4) and (5) are, in general, not separable. For orthogonal co-ordinates the metric elements are related to the scale factors as $\sqrt{g_{11}} = h_1$ and $\sqrt{g_{22}} = h_2$; hence the metric coefficients $g_{11}/\sqrt{g}$ and $g_{22}/\sqrt{g}$ can be written as

$$\frac{g_{11}}{\sqrt{g}} = \sqrt{\frac{g_{11}}{g_{22}}} = \frac{h_1}{h_2} \quad \text{and} \quad \frac{g_{22}}{\sqrt{g}} = \sqrt{\frac{g_{22}}{g_{11}}} = \frac{h_2}{h_1}. \tag{6d, e}$$

These ratios in equations (6d, e) represent the aspect ratio of a general curvilinear element in the physical plane corresponding to an infinitesimal square element in the transformed plane. Also, the elemental area $\mathrm{d}A$ in the physical plane is related to the corresponding area in the transformed plane as $\mathrm{d}A = \sqrt{g}\,\mathrm{d}\xi^1\,\mathrm{d}\xi^2$.

Use of equations (4) and (5), together with appropriate boundary conditions for ω and ψ, can lead to the formulation of an appropriate boundary value problem for the flow. However, the discussion on the boundary conditions will be deferred until the model flow problem to be analysed has been selected. The governing equations (4) and (5) form a coupled set of non-linear equations and the numerical method used to obtain their solutions is discussed next.

3. NUMERICAL ANALYSIS OF THE DISCRETE EQUATIONS

3.1. Preliminaries

The co-ordinate transformation referred to in Section 2 is so chosen as to transform the physical region R to a unit square in the computational plane (ξ^1, ξ^2). A uniform $(N + 1,$

$M + 1$) finite difference grid Δ is used and is defined as

$$\Delta = \{(\xi_i^1, \xi_j^2) \mid \xi_i^1 = i(\Delta\xi^1), \xi_j^2 = j(\Delta\xi^2)\}; \quad 0 \le i \le N + 1,\ 0 \le j \le M + 1, \tag{7}$$

with

$$\Delta\xi^1 = \frac{1}{N+1} \quad \text{and} \quad \Delta\xi^2 = \frac{1}{M+1}.$$

Thus the region R is comprised of $N + 1$ and $M + 1$ computational intervals along the ξ^1 and ξ^2 co-ordinate directions respectively. The cell aspect ratio β in the computational plane is given as $\beta = (\Delta\xi^1/\Delta\xi^2)$ and is maintained constant. For convenience, the following nomenclature is introduced for the metric coefficients:

$$G = \sqrt{g}, \qquad G11 = g_{11}/\sqrt{g} = \sqrt{(g_{11}/g_{22})}, \qquad G22\beta = g_{22}/\sqrt{g}\beta^2, \qquad G22 = \sqrt{g_{22}}/\sqrt{g_{11}}. \tag{8}$$

The spatial derivatives are approximated by appropriate finite difference quotients, using at most three grid points in a given direction. Keeping the spatial differences compact facilitates the implementation of the boundary conditions to second-order accuracy and aids in the overall stability of the algorithm. Consequently, central differences are used for both convective and diffusive derivatives in the governing equations. It is significant to note that, in this study, even with central difference approximations for all spatial derivatives, no artificial dissipation is added to dampen the high-frequency errors, but the latter are carefully annihilated through appropriate resolution of the various length scales of the problem.

3.2. Alternating direction implicit (ADI) method for vorticity transport equation

The conservative form of the two-dimensional vorticity transport equation (4) is differenced using a uniform ($N + 1$, $M + 1$) grid Δ defined by equation (7) and the resulting non-linear algebraic equations are solved using the ADI technique as described by Osswald and Ghia.[14] In this method the transport equation at time level t_{n+1} is discretized with the streamfunction being frozen at the time level t_n. As a result of this linearization, the formal temporal accuracy of the scheme is $O(\Delta t_n)$. For spatial discretization, a typical computational cell is shown sketched in Figure 1. For consistent differencing of the conservation form of the differential equations, the metric coefficients $(G11)_{i,j}$ and $(G22\beta)_{i,j}$ are evaluated at the staggered half-grid point locations, whereas the metric coefficient $G_{i,j}$, the solution field functions $\omega_{i,j}$, $\psi_{i,j}$ and the source term $q_{i,j}$ are evaluated at the cell corners. The ADI form of the discrete equations is arrived at by approximate factorization, which simplifies the computational algorithm to a sequence of one-dimensional solution processes. First, the intermediate vorticity field $\omega_{i,j}^*$, with its appropriate boundary conditions, is described by a tridiagonal matrix problem. Similarly, the final

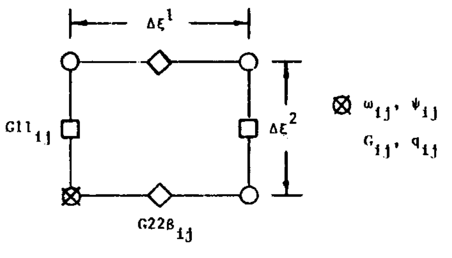

Figure 1. Typical computational cell and location of variables

vorticity $\omega_{i,j}^{n+1}$, with its own boundary conditions, forms a second tridiagonal matrix problem. These matrix problems are solved sequentially using the Thomas algorithm, which is a special form of the direct Gaussian elimination procedure. This calculation requires $28(N\cdot M)+24(N)$ floating point multiplications. The solution of the discrete transport equation provides a transient flow simulation with a formal truncation accuracy $O[\Delta t_n, (\Delta\xi^1)^2, (\Delta\xi^2)^2]$.

3.3. *Block Gaussian elimination (BGE) method*

For the solution of the discrete Poisson problem on a rectangular domain, considerable effort has been focused on the efficient direct methods of Buneman and Hockney as presented in References 16–19 using Cartesian co-ordinates. Schumann and Sweet[20] extended Buneman's cyclic reduction technique to include a very special class of separable non-Cartesian co-ordinates, whereas Schwarztrauber[21] has provided the extension of Buneman's method to treat the general separable elliptic equation. For the discrete Poisson problem in completely general orthogonal co-ordinates, Osswald and Ghia[14] have provided the highly competitive direct block Gaussian elimination method, which is accurate and efficient and is briefly summarized next.

3.3.1. The matrix Dirichlet Poisson problem in generalized orthogonal co-ordinates. The Dirichlet Poisson problem is formulated using a general scalar field function ϕ in some arbitrary orthogonal curvilinear co-ordinate system (ξ^1, ξ^2) such that

$$\frac{\partial}{\partial\xi^1}\left(\frac{g_{22}}{\sqrt{g}}\frac{\partial\phi}{\partial\xi^1}\right)+\frac{\partial}{\partial\xi^2}\left(\frac{g_{11}}{\sqrt{g}}\frac{\partial\phi}{\partial\xi^2}\right)=\sqrt{g}\,s(\xi^1,\xi^2)\quad\text{in } R, \tag{9a}$$

with

$$\phi = d(\xi^1,\xi^2)\quad\text{on}\quad \partial R. \tag{9b}$$

In this equation $s(\xi^1, \xi^2)$ is the known source term and $d(\xi^1, \xi^2)$ represents the given Dirichlet boundary conditions. Use of the grid Δ and central difference approximations for the spatial derivatives appearing in equation (9a) results in the discretized equation

$$\begin{aligned} &G22\beta_{i-1,j}\phi_{i-1,j}+G11_{i,j-1}\phi_{i,j-1}-(G22\beta_{i-1,j}+G11_{i,j-1}+G11_{i,j}+G22\beta_{i,j})\phi_{i,j}\\ &\qquad +G11_{i,j}\phi_{i,j+1}+G22\beta_{i,j}\phi_{i+1,j}=(\Delta\xi^2)^2G_{i,j}s_{i,j}. \end{aligned} \tag{10}$$

The Dirichlet boundary conditions are given as

$$\phi_{i,j}=d_{i,j}=d(\xi^1_i,\xi^2_j)\quad\text{on}\quad\partial\Delta. \tag{11}$$

The formal truncation accuracy of equation (10) is $O[(\Delta\xi^1)^2, (\Delta\xi^2)^2]$. Equation (10) can be written symbolically in matrix–vector form as

$$\mathbf{AP}=\mathbf{S}. \tag{12}$$

The coefficient matrix $\mathbf{A}$ in equation (12) is a symmetric $(N\times N)$ block tridiagonal matrix of the form

$$\mathbf{A}=\begin{bmatrix} \mathbf{A}_1 & \mathbf{B}_1 & \mathbf{0} & \mathbf{0} & \dots & \mathbf{0} & \mathbf{0}\\ \mathbf{B}_1 & \mathbf{A}_2 & \mathbf{B}_2 & \mathbf{0} & & \mathbf{0} & \mathbf{0}\\ \mathbf{0} & \mathbf{B}_2 & \mathbf{A}_3 & \mathbf{B}_3 & & \mathbf{0} & \mathbf{0}\\ & & & & & & \vdots\\ & & & & & \mathbf{B}_{N-1} & \mathbf{A}_N \end{bmatrix}, \tag{13a}$$

where the individual blocks $\mathbf{A}_i$ and $\mathbf{B}_i$ are square $(M \times M)$ submatrices dependent only upon the metric coefficients of the transformation given in equation (8). In particular, the diagonal blocks of $\mathbf{A}$ are the symmetric $(M \times M)$ tridiagonal matrices given as

$$\mathbf{A}_i = \begin{bmatrix} a_{i,1} & G11_{i,1} & 0 & 0 & \dots & 0 & 0 \\ G11_{i,1} & a_{i,2} & G11_{i,2} & 0 & & 0 & 0 \\ 0 & G11_{i,2} & a_{i,3} & G11_{i,3} & & 0 & 0 \\ \vdots & & & & & \vdots & \vdots \\ 0 & 0 & 0 & 0 & \dots & G11_{i,M-1} & a_{i,M} \end{bmatrix}, \tag{13b}$$

where the diagonal elements of $\mathbf{A}_i$ are given as

$$a_{i,j} = -(G22\beta_{i-1,j} + G11_{i,j-1} + G11_{i,j} + G22\beta_{i,j}). \tag{13c}$$

Further, the off-diagonal blocks of $\mathbf{A}$ are the $(M \times M)$ diagonal matrices given as

$$\mathbf{B}_i = \begin{bmatrix} G22\beta_{i,1} & & & & \\ & G22\beta_{i,2} & & & \\ & & G22\beta_{i,3} & & \\ & & & \ddots & \\ & & & & G22\beta_{i,M} \end{bmatrix}. \tag{13d}$$

To arrive at the form of the matrix–vector equation represented by equation (12), the unknown solution field $\phi_{i,j}$ has been arranged as a block vector $\mathbf{P}$ such that the individual block entries of $\mathbf{P}$ are the column vectors of the matrix $\phi_{i,j}$. This is expressed as

$$\mathbf{P} = (\mathbf{P}_1, \mathbf{P}_2, \dots, \mathbf{P}_N)^{\mathrm{T}}, \tag{14a}$$

where

$$\mathbf{P}_i = (\phi_{i,1}, \phi_{i,2}, \dots, \phi_{i,M})^{\mathrm{T}}. \tag{14b}$$

Thus the block vector $\mathbf{P}$ contains a total of $(N \cdot M)$ unknowns. Similarly, the source vector $\mathbf{S}$ is given as

$$\mathbf{S} = (\mathbf{S}_1, \mathbf{S}_2, \dots, \mathbf{S}_N)^{\mathrm{T}}, \tag{15a}$$

where

$$\mathbf{S}_i = (q_{i,1}, q_{i,2}, \dots, q_{i,M})^{\mathrm{T}} \tag{15b}$$

with

$$q_{i,j} = (\Delta\xi^2)^2 G_{i,j} s_{i,j} - \delta_{i1} G22\beta_{0,j} d_{0,j} - \delta_{iN} G22\beta_{N,j} d_{N+1,j} - \delta_{1j} G11_{i,0} d_{i,0} - \delta_{Mj} G11_{i,M} d_{i,M+1}. \tag{15c}$$

Here δ_{kl} is the Kronecker delta function.

Equation (13) shows that each diagonal block element $\mathbf{A}_i$ of the matrix Dirichlet Poisson operator $\mathbf{A}$ is itself diagonally dominant. Also, since the metric coefficients of equation (8) are always positive for any admissible co-ordinate transformation, each block element $\mathbf{A}_i$ will be negative definite and, consequently, non-singular. Such a symmetric block tridiagonal matrix, whose diagonal blocks are tridiagonal submatrices and whose off-diagonal blocks are diagonal submatrices, is very well suited for efficient direct inversion by the BGE technique of Osswald and Ghia[14] as described next.

3.3.2. The BGE technique for the Dirichlet Poisson problem. The block Gaussian elimination technique is an extension of the Gaussian elimination procedure to matrices whose individual elements are themselves matrices or blocks. The efficiency of the block elimination approach is enhanced when the block matrix is sparse. The BGE technique provides the effective inversion of an $(N\cdot M \times N\cdot M)$ matrix through the actual inversion of a predetermined sequence of N $(M \times M)$ subproblems.

The BGE approach naturally divides itself into two separate calculation phases. In the first phase a sequence of N $(M \times M)$ matrices is formed and individually inverted by simple scalar Gaussian elimination. This phase is the most time-consuming part of the calculation and the multiplication count performed shows that approximately $[\frac{1}{2}(N)(M)^3 + 2(N)(M)^2 - \frac{1}{2}(M)^3]$ floating point multiplications are required to complete this phase for the Dirichlet Poisson operator of equation (13a). Fortunately, this preliminary phase need be executed only once for a given co-ordinate choice, its result being permanently stored as a series of coefficient matrices for later use in the second phase of the block elimination procedure.

The second phase consists of the actual solution of the block matrix problem given by equation (12) for a prescribed source term **S** through a set of recursion relationships. These recursion relationships use the coefficient matrices precalculated in phase one and require approximately $[2(N)(M)^2 + 2(N)(M) - (M)^2]$ floating point multiplications. This count shows that the second phase of the procedure is far less time-consuming. Indeed, it is precisely because only the second phase of the BGE procedure need be repeated to solve equation (12) for various source terms that reasonable computational efficiency can be expected. This is particularly true in the context of an unsteady Navier–Stokes calculation during which the Dirichlet streamfunction Poisson problem must be solved many times in a given co-ordinate system for a progression of updated source terms.

It is important to note that the difference between the technique of Osswald and Ghia[14] described above and the block Gaussian elimination algorithm given by Dorr[17] is the recognition of the natural splitting of the BGE method into two separate phases. Indeed, it is precisely this splitting which allows the block Gaussian elimination procedure to remain competitive with other techniques available for the solution of the Dirichlet Poisson problem for the streamfunction ψ.

In view of this discussion, it should be stated that the combined ADI–BGE method developed here is very well suited for studying unsteady flows governed by the unsteady Navier–Stokes equations; it is also useful in obtaining time-asymptotic solutions of the steady Navier–Stokes equations.

4. MODEL PROBLEM FOR INCOMPRESSIBLE SEPARATED FLOW

The separation phenomena caused by abrupt changes in flow geometries in internal flows are well known. Any insight gained for this class of separated flows will lead to improved analyses and will aid in developing effective design tools. In general, separated flows become unstable at relatively moderate Reynolds number and an unsteady analysis which can accurately predict these types of flows would be most desirable. The flow over a backward facing step inside a channel has been used by many investigators as a model problem for viscous separated flow, owing to the simplicity of the geometry. Careful experimental data[22, 23] as well as numerical analyses[24, 25] are available for this flow. Hence this configuration has also been used in the present study of incompressible separated flow.

4.1. Details of Geometry and transformations

Figure 2 shows the configuration of a backward facing step inside a doubly infinite channel. For brevity, the configuration will be referred to as a backstep channel. The origin of the physical plane co-ordinates is placed at the location of the step transition. The channel height at the outlet is chosen as the reference length L_r and the mean outflow velocity is taken as the reference velocity U_r. Therefore the Reynolds number is defined as $Re = \rho U_r L_r/\mu$. Clearly, this flow configuration has a geometric similarity parameter H as shown in Figure 2. Here H is the ratio of the throat opening or pre-transition channel height to the post-transition channel height and may be viewed as a throttling mechanism for reference outflow conditions. The mean velocity U_{in} at inlet is related to the outflow velocity by the relation $U_{\text{in}} = U_r/H$. Thus, for fixed outflow conditions, diminishing the throat opening, i.e. decreasing H, will increase the mean inflow velocity and, subsequently, produce a larger separated flow field at fixed Re. Hence similarity for the backstep channel requires not only Reynolds number equality but also equality of the throat opening ratio H, which is bounded between 0 and 1.

4.1.1. Conformal transformation—T_B. The 'natural' co-ordinate system for the backstep channel is obtained using an analytical conformal transformation. This co-ordinate transformation is not only convenient to align the boundaries of the channel with the new curvilinear co-ordinates, but also allows accurate implementation of the boundary conditions while maintaining formal second-order spatial accuracy. The desired conformal transformation T_B is given by the relation

$$z = \frac{1}{\pi}\{\ln[U + (U^2 - 1)^{1/2}] - H\ln[V + (V^2 - 1)^{1/2}]\}. \tag{16a}$$

The various quantities appearing in this equation, as well as those used in subsequent definitions, are given as

$$U = \frac{2W - (k+1)}{k-1}, \qquad V = \frac{(k+1)W - 2k}{(k-1)W}, \qquad W = e^{\pi\zeta}, \qquad k = \left(\frac{1}{H}\right)^2,$$
$$\zeta = \eta^1 + i\eta^2, \qquad z = x + iy \qquad \text{and} \qquad i = \sqrt{(-1)}. \tag{16b}$$

This transformation maps the doubly infinite backstep channel geometry of Figure 2 onto a doubly infinite strip $[(\eta^1, \eta^2) | -\infty \le \eta^1 \le +\infty, 0 \le \eta^2 \le 1]$ in the conformal (η^1, η^2) plane. An additional transformation is needed to make the domain in the η^1 direction bounded for computational purposes.

4.1.2. Grid-clustering transformation—T_C. A second transformation is used to map this doubly infinite strip in the (η^1, η^2) plane onto a unit square in the computational domain R. Here two

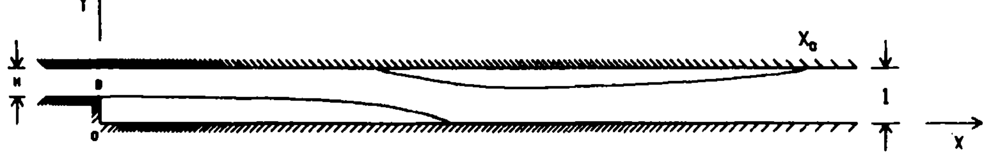

Figure 2. Backstep channel geometry

independent one-dimensional stretching transformations are used to provide the desired grid clustering in the boundary layers and separated regions of the flow field. The use of two separate 1D stretching transformations provides the flexibility needed to resolve the multiple scales of this flow problem. These grid-clustering transformations are given as

$$\xi^1 = \frac{1}{2\pi}\left[\tan^{-1}\left(\frac{\eta^1-\alpha_1}{D_1}\right)+\tan^{-1}\left(\frac{\eta^1-\alpha_2}{D_2}\right)\right]+\frac{1}{2}, \tag{17a}$$

$$\xi^2 = \left[2\tan\left(\frac{1}{2c}\right)\right]^{-1}\tan\left(\frac{\eta^2-\frac{1}{2}}{c}\right)+\frac{1}{2}. \tag{17b}$$

The parameters α_1 and α_2 represent the two η^1 locations where grid points are to be clustered in the streamwise direction, while the parameters D_1 and D_2 control the degree of this clustering. Similarly, the parameter c controls the degree of gridpoint clustering in the normal direction. The degree of clustering can also be interpreted in terms of a stretching ratio SR; e.g., for the normal co-ordinate clustering,

$$\mathrm{SR} \sim \left.\frac{\mathrm{d}(\xi^2)}{\mathrm{d}(\eta^2)}\right|_{\eta^2=0,1}.$$

4.1.3. Combined transformation—$T=T_{\mathrm{B}}\cdot T_{\mathrm{C}}$. The metric coefficients given in equation (8) can now be determined for the overall co-ordinate transformation, which is obtained by combining the transformations T_{B} and T_{C} given in equations (16) and (17). The metric coefficients become

$$G = h^2\gamma_1(\eta^1)\gamma_2(\xi^2), \tag{18a}$$

$$G11 = \gamma_1(\eta^1)/\gamma_2(\xi^2) \tag{18b}$$

and

$$G22 = \gamma_2(\xi^2)/\gamma_1(\eta^1). \tag{18c}$$

The quantities $\gamma_1(\eta^1)$ and $\gamma_2(\xi^2)$ are defined as

$$\gamma_1(\eta^1) = 2\pi\Big/\left(\frac{D_1}{D_1^2+(\eta^1-\alpha_1)^2}+\frac{D_2}{D_2^2+(\eta^1-\alpha_2)^2}\right) \tag{19a}$$

and

$$\gamma_2(\xi^2) = 2c\tan(1/2c)/\{1+[2(\xi^2-\tfrac{1}{2})\tan(1/2c)]^2\}, \tag{19b}$$

and h is the scale factor of the conformal transformation given as

$$h = \left|\frac{\mathrm{d}z}{\mathrm{d}\zeta}\right|. \tag{19c}$$

For the overall transformation given in equations (18), γ_1 is a function of η^1 only and γ_2 depends only on ξ^2. In this sense the co-ordinate transformation is considered separable. Indeed, this was expected because of the choice of the individual transformations T_{B} and T_{C}. However, it should be noted that the analysis developed here is valid even when the co-ordinate transformation is merely orthogonal, i.e. neither conformal nor separable in the sense just stated.

4.2. Selection of transformation parameters to resolve multiple scales

For the backstep channel geometry as shown in Figure 2, the region extending from slightly upstream of the backward facing step to the farthest reattachment point is referred to as the 'transition' region. In this region, convection dominates over diffusion. On the other hand, the regions upstream and downstream of this 'transition' region become increasingly diffusion-dominated as the inlet and outlet sections at ± ∞ of the channel are approached. In an experimental study of the 'transition' region of the backstep channel geometry, Armaly and Durst[23] have shown the existence of one or more separation bubbles in the channel, for a fixed value of H, as the value of Re is increased gradually. If such a separated flow has to be computed accurately, the scaling in the normal direction is no longer $O(Re^{-1/2})$. At high Re the correct scaling[3, 4] for the separated flow around the separation points is $O(Re^{-3/8})$ in the streamwise direction and $O(Re^{-5/8})$ in the normal direction.

In the grid-clustering transformation T_C five parameters ($\alpha_1, \alpha_2, D_1, D_2$ and SR) are embedded in equation (19). These parameters facilitate, to a reasonable extent, the desired grid clustering in the physical plane to resolve the multiple scales of this separated flow model problem. To resolve the scales in the streamwise direction near the separation points, the parameters D_1 and D_2 are chosen to provide the desired grid clustering around the proper locations α_1 and α_2, such that the separation scales $O(Re^{-3/8})$ in the streamwise direction are appropriately resolved. The mathematical expressions which determine these four parameters are given as

$$\alpha_1 = \frac{\ln(k)}{\pi}, \tag{20a}$$

$$\alpha_2 = \alpha_1 + c_1\left(\frac{\ln(W_{X_0})}{\pi} - \alpha_1\right), \tag{20b}$$

$$D_1 = \alpha_1 \Big/ \tan\left[2\pi m_1 \Delta\xi^1 + \tan^{-1}\left(\frac{\alpha_2 - \alpha_1}{D_2}\right) - \tan^{-1}\left(\frac{\alpha_2}{D_2}\right)\right] \tag{20c}$$

and

$$D_2 = (\alpha_2 - \alpha_1)/\tan[2\pi m_2 + (m_2 - m_3)\Delta\xi^1]. \tag{20d}$$

Here m_1 is an integer denoting the number of $\Delta\xi^1$ intervals placed on the step height BO and m_3 is the total number of $\Delta\xi^1$ intervals between the inflow boundary and point O. The quantity m_2 is taken to be 1/2 in order to map the points B and O onto midpoints of $\Delta\xi^1$ intervals; this allows for circumventing the singularity in the metric coefficients at these corner points. The values selected for m_1 and m_3 are such that the resulting overall grid satisfies two requirements. First, between the corner point B and the reattachment point X_0, the streamwise grid spacing is required to be nearly uniform as the distance BX_0 is a measure of the convection scale. Secondly, the near-infinity diffusion scale must also be resolved. Hence the grid is stretched in the streamwise direction only after the flow has become diffusion-dominated.

In the normal direction the parameter SR aids in resolving the scales $O(Re^{-5/8})$ around the lower and upper separation points as well as the wall shear layers. The actual choice of a particular grid for a given configuration is arrived at by numerical experiments with the grid generator in which the various parameters are selected so as to yield the desired grid. The grid distributions used in this study will be presented in the next section.

4.3. Asymptotic flow near channel infinities

The analysis to be presented here is valid for a class of internal flow problems in which the normal co-ordinate η^2 is bounded and, asymptotically at $\eta^1 = \mp\infty$, the configurations have straight inflow and outflow sections, with any desired shape of the connecting transition section. The grid-clustering transformation T_C was selected so as to map the inflow and outflow boundary conditions at $\pm\infty$ to the finite values $\xi^1 = 0$ and $\xi^1 = 1$ respectively in the computational co-ordinates. Consequently, $1/\eta^1$ becomes a small parameter in the proximity of the inflow section, where $\xi^1 = 0$, and near the outflow section, where $\xi^1 = 1$. With the use of a small parameter defined as

$$\varepsilon = 1/\eta^1, \tag{21}$$

Osswald[26] has determined the scale factor h near the inflow and outflow sections and has shown that

$$\text{as } \eta^1 \to -\infty\text{:} \quad h = H - H\cos(\pi\eta^2)\left(\frac{k-1}{2k}\right)e^{\pi/\varepsilon} + O(e^{\pi/\varepsilon})^2 \tag{22a}$$

and

$$\text{as } \eta^1 \to +\infty\text{:} \quad h = 1 - \cos(\pi\eta^2)\left(\frac{k-1}{2}\right)e^{-\pi/\varepsilon} + O(e^{-\pi/\varepsilon})^2. \tag{22b}$$

Thus the backstep channel approaches a straight channel near the inflow and outflow sections in an exponential manner. Near these sections the function γ_1 of equation (19a) takes the form

$$\gamma_1 = \frac{2\pi}{D_1 + D_2}\left(\frac{1}{\varepsilon}\right)^2 - \frac{4\pi(\alpha_1 D_1 + \alpha_2 D_2)}{(D_1 + D_2)^2}\left(\frac{1}{\varepsilon}\right) + O(1), \tag{23}$$

whereas the function γ_2 of equation (19b) remains unaffected. Considering only the leading term in equation (23) yields $\gamma_1 = \Gamma_\infty(1/\varepsilon)^2$, where $\Gamma_\infty = \text{const}$. This asymptotic behaviour of γ_1 is representative of the wide class of internal flow problems referred to at the beginning of this subsection.

The grid-clustering transformation T_C maps the region $-\infty < \eta^1 < \infty$ onto the interval [0, 1] in the ξ^1 direction in such a manner that η^1 approaches infinity like $1/\varepsilon$. Hence the metric coefficients given in equations (18) take the form

$$G = h_\infty^2 \Gamma_\infty \gamma_2 \left(\frac{1}{\varepsilon}\right)^2 - O\left(\frac{1}{\varepsilon}\right), \tag{24a}$$

$$G11 = \frac{\Gamma_\infty}{\gamma_2}\left(\frac{1}{\varepsilon}\right)^2 - O\left(\frac{1}{\varepsilon}\right) \tag{24b}$$

and

$$G22 = \frac{\gamma_2}{\Gamma_\infty}(\varepsilon)^2 + O(\varepsilon^3), \tag{24c}$$

where

$$h_\infty = \lim_{\xi^1 \to 0,1} [h] \qquad \text{and} \qquad \Gamma_\infty = \lim_{\eta^1 \to \pm\infty}\left[\frac{\gamma_1}{(\eta^1)^2}\right] = \frac{2\pi}{D_1 + D_2}. \tag{25a, b}$$

In the light of this analysis, the governing differential equations (4) and (5) take the following form near upstream and downstream infinity:

$$\left[\frac{\varepsilon^2}{h_\infty^2 \Gamma_\infty \gamma_2} + O(\varepsilon^3)\right]\frac{\partial}{\partial \xi^1}\left[\frac{\gamma_2 \varepsilon^2}{\Gamma_\infty}\frac{\partial \psi}{\partial \xi^1} + O(\varepsilon^3)\frac{\partial \psi}{\partial \xi^1}\right] + \left[\frac{\varepsilon^2}{h_\infty^2 \Gamma_\infty \gamma_2} + O(\varepsilon^3)\right]\frac{\partial}{\partial \xi^2}\left[\frac{\Gamma_\infty}{\gamma_2 \varepsilon^2}\frac{\partial \psi}{\partial \xi^2} - O\left(\frac{1}{\varepsilon}\right)\frac{\partial \psi}{\partial \xi^2}\right] = -\omega, \tag{26a}$$

$$\begin{aligned} \frac{\partial \omega}{\partial t} &+ \left[\frac{\varepsilon^2}{h_\infty^2 \Gamma_\infty \gamma_2} + O(\varepsilon^3)\right]\left[\frac{\partial}{\partial \xi^1}\left(\omega \frac{\partial \psi}{\partial \xi^2}\right) - \frac{\partial}{\partial \xi^2}\left(\omega \frac{\partial \psi}{\partial \xi^1}\right)\right] \\ &= \frac{1}{Re}\left[\frac{\varepsilon^2}{h_\infty^2 \Gamma_\infty \gamma_2} + O(\varepsilon^3)\right]\frac{\partial}{\partial \xi^1}\left[\frac{\gamma_2 \varepsilon^2}{\Gamma_\infty}\frac{\partial \omega}{\partial \xi^1} + O(\varepsilon^3)\frac{\partial \omega}{\partial \xi^1}\right] \\ &\quad + \frac{1}{Re}\left[\frac{\varepsilon^2}{h_\infty^2 \Gamma_\infty \gamma_2} + O(\varepsilon^3)\right]\frac{\partial}{\partial \xi^2}\left[\frac{\Gamma_\infty}{\gamma_2 \varepsilon^2}\frac{\partial \omega}{\partial \xi^2} - O\left(\frac{1}{\varepsilon}\right)\frac{\partial \omega}{\partial \xi^2}\right]. \end{aligned} \tag{26b}$$

Since η^1 is a function of ξ^1 only,

$$\frac{\partial}{\partial \xi^1}(\varepsilon^2) = -2\varepsilon^3\left(\frac{d\eta^1}{d\xi^1}\right) = -2\varepsilon^3\gamma_1 = -2\Gamma_\infty\varepsilon + O(\varepsilon^2) \tag{27a}$$

and

$$\frac{\partial}{\partial \xi^2}\left(\frac{1}{\varepsilon^2}\right) = 0. \tag{27b}$$

Thus equations (26) simplify to the following form near the channel inflow and outflow sections:

$$\frac{\partial \omega}{\partial t} = \frac{1}{Re h_\infty^2 \gamma_2}\frac{\partial}{\partial \xi^2}\left[\frac{1}{\gamma_2}\frac{\partial \omega}{\partial \xi^2}\right] + O(\varepsilon) \tag{28a}$$

and

$$\frac{1}{h_\infty^2 \gamma_2}\frac{\partial}{\partial \xi^2}\left[\frac{1}{\gamma_2}\frac{\partial \psi}{\partial \xi^2}\right] = -\omega + O(\varepsilon). \tag{28b}$$

It is observed that equations (26) are ξ^2 diffusion-dominated near channel inflow and outflow sections. The most significant terms, namely, those $O(1)$ as well as $O(\varepsilon)$, are associated with the ξ^2 diffusion operator, whereas the convection terms are $O(\varepsilon^2)$ and the ξ^1 diffusion terms are $O(\varepsilon^3)$. If terms $O(\varepsilon)$ are to be considered negligible in the asymptotic equations (27), η^1 must be large enough such that $\eta^1 \sim O(1/\varepsilon)$. For large η^1 the present class of geometrical configurations is such that $x^1 \sim \eta^1$. Hence there exist regions $O(1/\varepsilon)$ in the physical plane near the inflow and outflow boundaries in which the flow simply diffuses in the ξ^2 direction normal to the channel walls. These regions isolate the infinity boundaries from the convection-dominated transition region since any disturbance entering these regions is totally damped within the regions. Equations (28) enable plane Poiseuille flow to be established near the inlet and outlet sections, without any special treatment of the interior difference operators at these boundaries.

4.4. Boundary and initial conditions

To maintain consistent second-order spatial accuracy of the overall solution, the wall vorticity boundary conditions must also be implemented with second-order spatial accuracy. The earlier analysis of Ghia *et al.*[27] was generalized by Osswald[26] to provide the second-order-accurate form of the wall vorticity boundary condition. This analysis expands the function $\partial\psi/\partial\xi^2$ at the midpoint of a boundary cell using a Taylor's series expansion in terms of the function and its derivatives at the boundary itself. The consistent treatment of the higher derivatives of $\partial\psi/\partial\xi^2$ at the boundary, including the use of the reduced form of the governing equation (5), leads to the desired expression for the wall vorticity. Thus the boundary conditions on the lower wall $\xi^2 = 0$ are

$$(\Delta\xi^2)^2[3G_L\omega_L + G_{L+1}\omega_{L+1}] = 8G11_{L+1/2}\frac{[\psi_{L+3} - 3\psi_{L+2} - 21\psi_{L+1} + 23\psi_L]}{24} - (\Delta\xi^2)^2\frac{\partial}{\partial\xi^1}\left[G22\frac{\partial\psi}{\partial\xi^1}\right]_{L+1} + O(\Delta\xi^2)^4 \tag{29a}$$

and

$$\psi_L = 0. \tag{29b}$$

A similar expression can be obtained for the vorticity at the upper wall $\xi^2 = 1$, where the streamfunction $\psi_U = 1$.

The boundary conditions for ω and ψ at inflow and outflow sections are determined from the asymptotic form of the governing differential equations. These are obtained from equations (28) as

$$\frac{\partial \omega}{\partial t} = \frac{1}{Re h_\infty^2 \gamma_2} \frac{\partial}{\partial \xi^2} \left[\frac{1}{\gamma_2} \frac{\partial \omega}{\partial \xi^2} \right] \tag{30a}$$

and

$$\frac{1}{h_\infty^2 \gamma_2} \frac{\partial}{\partial \xi^2} \left[\frac{1}{\gamma_2} \frac{\partial \psi}{\partial \xi^2} \right] = -\omega. \tag{30b}$$

For consistency with the numerical solutions in the interior, numerical rather than analytical solutions of the steady form of equations (30) are used to provide the boundary conditions for ω and ψ at the inflow and outflow sections. The appropriate wall boundary conditions for these asymptotic equations are obtained from equations (29) by dropping out the ξ^1 derivative term. Equations (30a, b) were solved simultaneously using a block Gaussian elimination method, which in effect is identical to solution by a modified Thomas algorithm for this coupled set of equations.

For the initial conditions the flow inside the backstep channel was assumed, everywhere, to consist of the numerical solution of the steady form of equations (30) obtained at $\eta^1 \to \pm \infty$. In the physical plane this corresponds to parabolic velocity distributions at $x^1 \to \pm \infty$, while in the region of the backstep these are scaled by the conformal transformation scale factor. This procedure avoids discontinuities in the initial conditions at the backstep.

5. RESULTS FOR BACKSTEP CHANNEL

The unsteady Navier–Stokes analysis and solution procedure discussed in Sections 2 and 3 are applied to the flow in a doubly infinite backstep channel. This separated flow problem has been classified by Kumar and Yajnik[28] to have a streamwise length scale L_x of $O(Re)$ and, in the limit of high Reynolds number, is governed by parabolic equations. This implies that the upstream influence is confined to a relatively short distance, whereas the extent of the region of downstream influence increases with Re. The singularity at the sharp convex corner, as well as the difficulties associated with the simulation of high-Re flows, have been addressed in the present analysis by exercising care in the formulation of the discretized problem. Hence the results obtained are anticipated to be accurate. For all of the flow configurations listed in Table I, the predicted results have asymptoted to steady state.

5.1. *Quality of grid*

Application to flow configurations for which experimental data are available, together with the fact that the Navier–Stokes equations (4) and (5) asymptote to the diffusion-dominated equations (30) near the inflow and outflow boundaries, aided in the choice of appropriate values for the parameters m_1 and m_3. Numerical experiments with various grids for these configurations enabled careful examination of the length scales near the separation points, as well as the near-infinity scale. This latter scale is assumed to be correctly represented if the flow solution in the interior smoothly approached the inflow and outflow boundary values. This requires that grid points be appropriately distributed in the diffusion-dominated regions near these boundaries. The degree to which the ξ^2 diffusion coefficient $G_{11}/G\,Re$ dominates over the convection coefficient G in the grid cells adjacent to these boundaries provides a quantitative measure of the appropriateness of the near-infinity grid point distribution. Hence a quantity Q is defined as

$$Q = \left. \frac{\text{convection}}{\xi^2 \text{ diffusion}} \right|_{\text{near infinity}} = \max \left[\frac{Re}{G11_{N,j}} \right] \tag{31}$$

Table I. Parameters for various flow configurations

Configuration	H	h_s	Re	Re_D	Re_S	L_1	L_4	L_5	$L_5 - L_4$	Reference
I	0·90000	0·10000	900	1800	100	0·69	—	—	—	Rubin and Khosla[33]
II	0·66667	0·33333	146	292	72	1·69	—	—	—	Denham and Patrick[22]
III			250	500	125	2·50	—	—	—	
IV			458	916	229	3·91	—	—	—	
V	0·51485	0·48515	150	300	141	3·23	—	—	—	Armaly and Durst[23]
VI			300	600	283	4·96	4·05	7·32	3·27	
VII			507	1014	478	6·08	4·70	11·45	6·75	
VIII			600	1200	565	6·39	4·97	12·96	7·99	

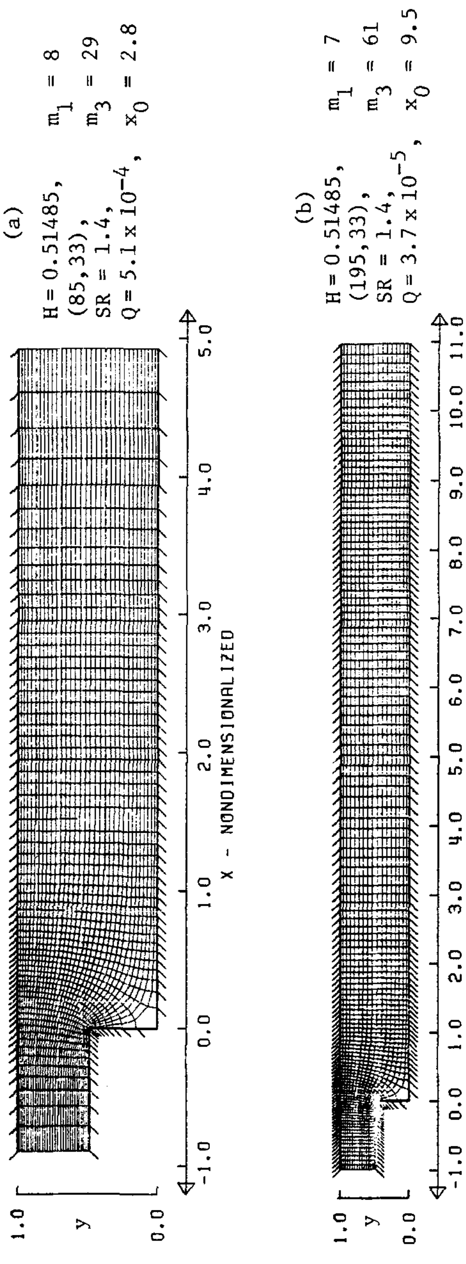

Figure 3. Typical grid distributions

and is required to be as small as possible near $\xi^1 = 0$ and 1. In the present study Q was monitored for each grid distribution used and maintained to be $O(10^{-3})$ or less. Two typical distributions with 85 × 33 and 195 × 33 grid points used in some of the present computations are shown in Figures 3(a) and (3b).

5.2. Criteria for steady state, accuracy and computational efficiency

The steady state results were generated, wherever possible, as the time-asymptotic limit of the unsteady analysis. The criterion used to define the steady state is given as

$$\left|\frac{f^{n+1}_{i,j}-f^{n}_{i,j}}{f^{n+1}_{i,j}\,\Delta t}\right|_{\max} < \varepsilon_f \quad \text{with} \quad \varepsilon_f = 10^{-4}, \tag{32}$$

where f represents either ω or ψ and the subscript max denotes the maximum value encountered in the grid Δ. It was observed that, in general, ψ converged much more rapidly than ω. Much before this criterion was satisfied everywhere, the flow in the 'transition' region settled at its steady state values, while the flow in the regions near the outflow boundary continued to adjust at rather slow rates until it finally satisfied equation (32). Hence the calculations were continued for almost twice as many characteristic time units as those required for steady state to be achieved in the transition region. In each case the numerical procedure continued to yield consistent and stable solutions.

Central differences are used throughout the flow field, so that the overall accuracy of the present method is $O[\Delta t, (\Delta\xi^1)^2, (\Delta\xi^2)^2]$. By satisfactorily resolving the multiple scales present in the problem, the resulting solutions are totally wiggle-free.

The relative computational efficiency of the present algorithm was measured in terms of the CPU time τ required to advance the solution by one time step per spatial grid point, i.e.

$$\tau = \frac{\text{CPU seconds}}{\text{number of mesh points} \times \text{number of time steps}},$$

where τ represents the 'computational effort'. For the present algorithm $\tau = 2{\cdot}67 \times 10^{-4}$ s for the AMDAHL 470 V/7 computer. The corresponding value for the implicit method of Beam and Warming[29] is $4{\cdot}4 \times 10^{-4}$ s for the compressible Navier–Stokes equations using the CDC 7600 computer.

5.3. Comparison of steady state flow results with experimental data

Table I shows the eight flow configurations which have been analysed in the present study. These include the configurations for which experimental data are available from Denham and Patrick[22] or Armaly and Durst.[23] The published experimental data provide one or more of the following results:

(i) stream line contours
(ii) velocity profiles at various streamwise locations using Cartesian co-ordinates
(iii) locations of separation and reattachment points.

The primary separation bubble off the backstep is characterized by the length of the eddy, i.e. by its corresponding reattachment length. This reattachment length is plotted versus Re in Figure 4(a), with the throat-opening ratio H as a parameter. The present results show a consistently longer primary reattachment length than was obtained experimentally by Denham and Patrick.[22] This discrepancy can be attributed to the fact that Denham and Patrick[22] placed an asymmetric flared device along the lower wall of an otherwise straight channel to form the backward facing step. As a result, the inlet section of their experimental configuration was relatively short, with $L_{IN}/H_{IN} = 3{\cdot}33$. Hence their velocity profiles just prior to the step show an asymmetric distortion from the very nearly parabolic velocity profiles seen in both the present numerical simulation and the experimental study of Armaly and Durst.[23] Indeed, the severity of the distortion in the inflow conditions of Denham and Patrick[22] increases with increasing Reynolds number. Furthermore, Denham and Patrick[22] have implied that the noticeable

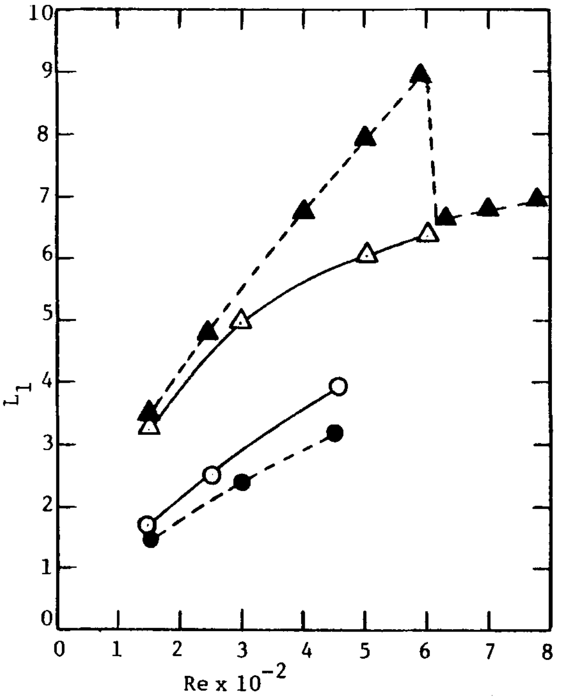

Figure 4(a). Reattachment length of separation bubble on lower wall

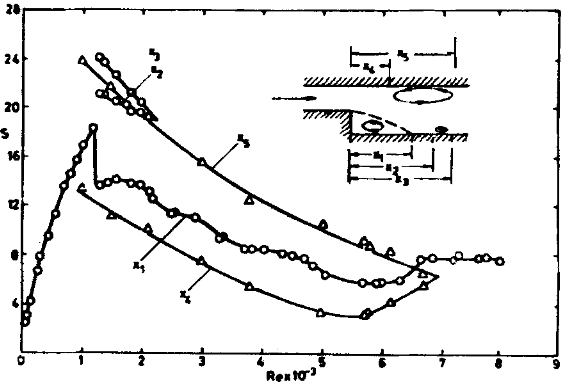

Figure 4(b). Circulation regions at the upper and lower walls (after Reference 23)

LEGEND FOR FIGURES 4a AND 4c

Ref. H	Present	Denham & Patrick [22]	Armaly & Durst [23]
0.51485	—△—		-▲-
0.66667	—○—	-●-	
0.90000	□		

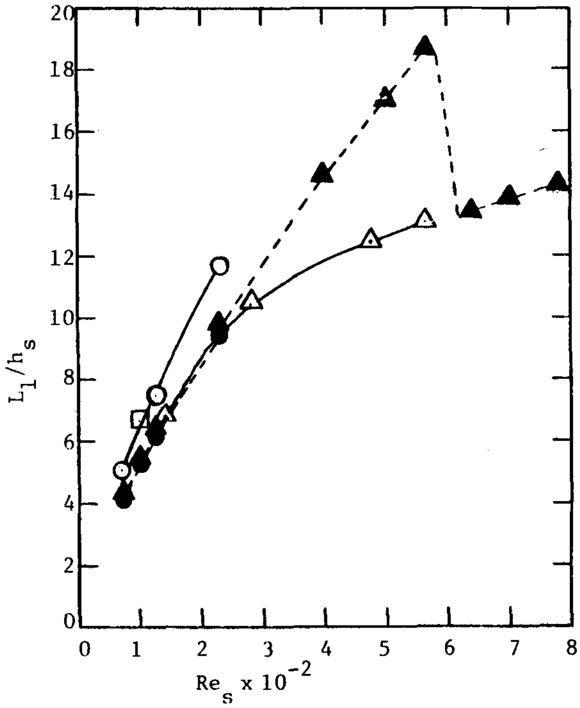

Figure 4(c). Similarity study for reattachment length

skewness of their inlet conditions could result in a tendency to shorten their measured reattachment lengths; this observation is consistent with the results of Figure 4(a). Finally, as seen from Table I, no secondary separation bubble forms along the upper channel wall for configurations with $H = 0{\cdot}66667$. This result is consistent with the experimental observations of Denham and Patrick[22] up to the highest Reynolds number $Re = 458$ or $Re_S = 229$ used in their investigation, where Re_S is based on h_S.

A direct comparison of the results of the present numerical analysis with the laser–Doppler experimental data of Armaly and Durst[23] is also presented in Figure 4. As seen here, the present two-dimensional steady state results are in excellent agreement with the experimental data of Armaly and Durst[23] provided that only the primary separation bubble exists within the flow field. Indeed, the agreement is excellent provided $Re \lesssim 225$ or, equivalently, $Re_S \lesssim 212$. More precisely, Table I indicates that the first appearance of the secondary separation bubble is bracketed between $Re = 150$ and $Re = 300$ and can be obtained by graphical extrapolation to be $Re \approx 200$. Since $Re = 200$ corresponds to $Re_S = 189$, the present numerical prediction for the first appearance of the secondary separation bubble is in excellent agreement with the experimentally observed value of $Re_S \approx 190$ quoted by Armaly *et al.*[30]

However, for $Re > 225$ the present two-dimensional results depart from the experimental observations of Armaly and Durst.[23] This departure is to be expected since Armaly *et al.*[30] have found evidence of three-dimensionality in the earlier data of Armaly and Durst[23] for $Re \gtrsim 200$. Indeed, they found that the onset of three-dimensionality coincided with the first occurrence of the secondary separation bubble. A possible mechanism for this abrupt change in flow structure is now presented.

Nominally, two-dimensional boundary layer flows subject to locally destabilizing concave curvature of the boundary wall are known to be susceptible to the classical Taylor–Görtler instability leading to the formation of spanwise-periodic pairs of counter-rotating vortices whose axes are aligned with the flow direction (see e.g. Smith[31]). Furthermore, Inger[32] suggested that such a vortex disturbance mechanism could be a common phenomenon near two-dimensional separation points, whenever the dividing streamline is inclined to the direction of the main flow by more than just a few degrees. By referring to Figures 5(c) and 5(d), it can be seen that such a condition on the dividing streamline is first met with the appearance of the secondary separation bubble along the upper channel wall. Below this 'critical' point, only the primary separation bubble exists within the channel; however, its dividing streamline separates essentially parallel to the main flow direction and is then subjected to stabilizing convex curvature as it drops and impinges upon the lower channel wall.

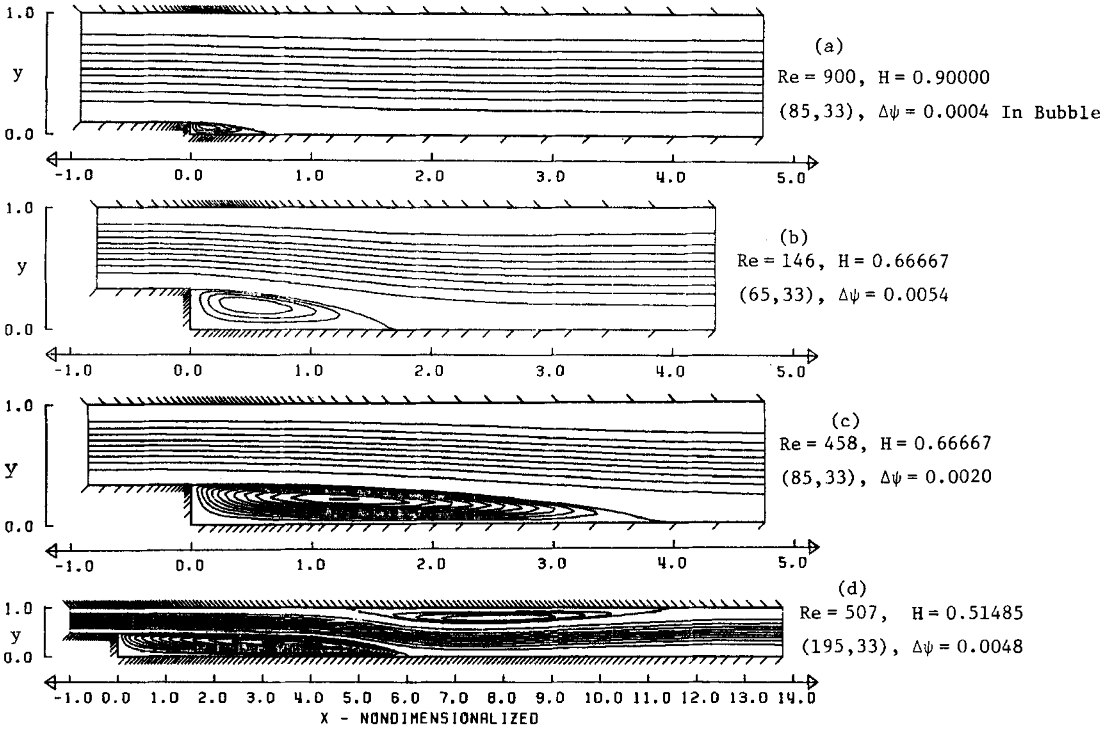

Figure 5. Steady state streamfunction contours; $\Delta\psi = 0{\cdot}1$

Such a vortex instability mechanism is consistent with the onset of three-dimensionality as described by Armaly *et al.*[30] Indeed, the increasing difference between the present calculations and measurements above $Re = 225$ can be interpreted as confirming the increasingly three-dimensional character of the experimental flow field.

An alternative mechanism also leading to three-dimensional effects in a nominally two-dimensional flow field is the growth and eventual interaction of the boundary layers on the sidewalls of the experimental apparatus. However, such an effect would tend to diminish with increasing Reynolds number as the sidewall boundary layers would then tend to become thinner. Thus a careful comparison between experiment and a two-dimensional flow calculation has led to important insight into the nature of separated viscous flows; this insight could have easily been missed or misinterpreted if one relied wholly on the experiment or on the calculations alone.

Additional support for the hypothesis that a Taylor–Görtler vortex instability mechanism associated with the secondary separation region is primarily responsible for the discrepancy between the measurements of Reference 23 and the present two-dimensional calculations for $Re \gtrsim 225$ can be obtained from the results presented in Table I. Specifically, it is suggested that the additional mixing which would accompany a developing Taylor–Görtler instability would tend to delay the upper wall separation, thus causing the secondary separation point L_4 to occur farther downstream than would be predicted on the basis of a strictly two-dimensional analysis. This would in turn decrease the blockage effect caused by the secondary separation bubble, thus allowing the primary separation bubble to elongate beyond the length predicted in the strict absence of any three-dimensional disturbance effect. Indeed, as seen in Figure 4, the flow exhibits exactly these characteristics for Re in the range 225–600.

5.4. Steady state results for various backstep flow configurations

The steady state results are presented here for flow configurations I, II, IV and VII with Re_D of 1800, 292, 916 and 1014 respectively. Figures 5(a) to 5(d) show the streamline contours for these configurations. As seen in Figure 5(a), configuration I with $Re_D = 1800$ is the one with the smallest separation bubble and hence is relatively simple to compute. This configuration was used by Rubin and Khosla[33] in the development of their coupled strongly implicit method. Figures 5(b) and 5(c) show the streamline contours for configuration II with $Re_D = 292$ and configuration IV with $Re_D = 916$ respectively. These configurations were used by Denham and Patrick[22] in their experimental study. As expected, the length of the separation bubble grows with increase in Re. Finally, the streamline contours are presented for configuration VII with $Re_D = 1014$ in Figure 5(d). This configuration was used by Armaly and Durst[23] in their study. To the authors' knowledge, the present results constitute the first detailed results computed for this flow problem showing a separation bubble on the upper wall. Results for these flows were first presented by the authors in 1983.[34] Also, persistently unsteady results are given by Osswald *et al.*[35] for $H = 0{\cdot}514\,85$, $Re_D = 4000$. Kim and Moin[36] applied a fractional step method to the backstep channel flow problem and showed the secondary separation on the upper wall for $Re = 600$.

The corresponding vorticity contours for the four configurations considered in Figure 5 are shown in Figures 6(a) to 6(d). As anticipated, a heavy concentration of contour lines occurs near the sharp convex corner, an indication of the presence of high vorticity gradients in this region of maximum generation of vorticity. In the 'transition' region the vorticity contours are swept downstream by the strong convection effects.

Figures 7(a) to 7(d) provide the transverse profiles of the total velocity vector, along ξ^2 lines, at selected streamwise locations. A region of reversed flow is observed downstream of the step near

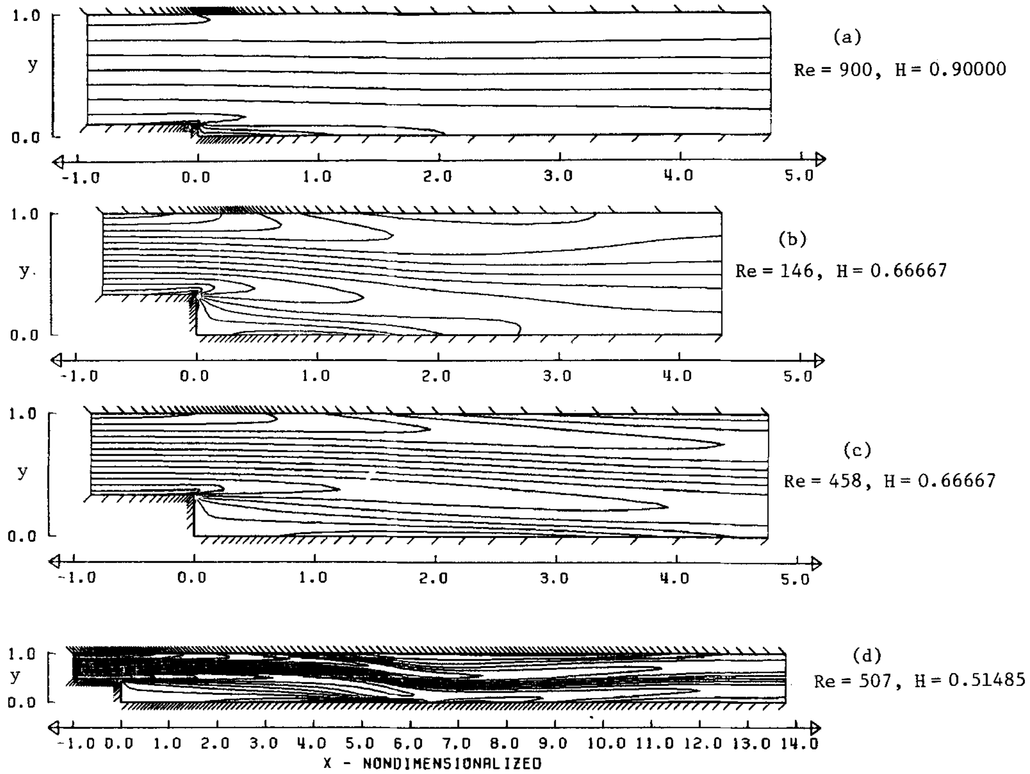

Figure 6. Steady state vorticity contours; $\Delta\omega = 2{\cdot}0$

the lower wall for all of these configurations. Configuration VII with $Re_D = 1014$, shown in Figure 7(d), exhibits a large region of reversed flow near the upper wall also.

5.5. Transient results for backstep flow configuration VIII

The transient results for flow configuration VIII with $Re_D = 1200$ are presented in Figure 8. Starting from time $t = 0$, four values of the characteristic time, namely 4, 40, 112 and 421, are chosen to depict the time history of the flow as it approaches steady state. The flow in the transition region reaches close to its steady state value at about $t = 76$, but the adjustments taking place near the outflow boundary require $t = 421$ in order to satisfy the steady state criterion of equation (32). Figures 8(a) to 8(d) show the streamline contours of this transient flow as it reaches steady state, while Figures 9(a) to 9(d) show the vorticity contours. As seen from the streamfunction contours of Figure 8 and especially from the vorticity contours of Figure 9, the early disturbance for $t \lesssim 4$ is localized near and just downstream of the backward facing step. Indeed, for $t = 4$ several large-scale coherent eddy structures have formed in the wake of the backward facing step along both the upper and lower channel walls. These eddies are seen to have transverse length scales of the order of the step height and penetrate approximately five outlet channel heights downstream of the step. In addition, the vorticity contours of Figure 9 indicate that a region of high convective mixing extends approximately five characteristic length units downstream of the step at $t = 4$.

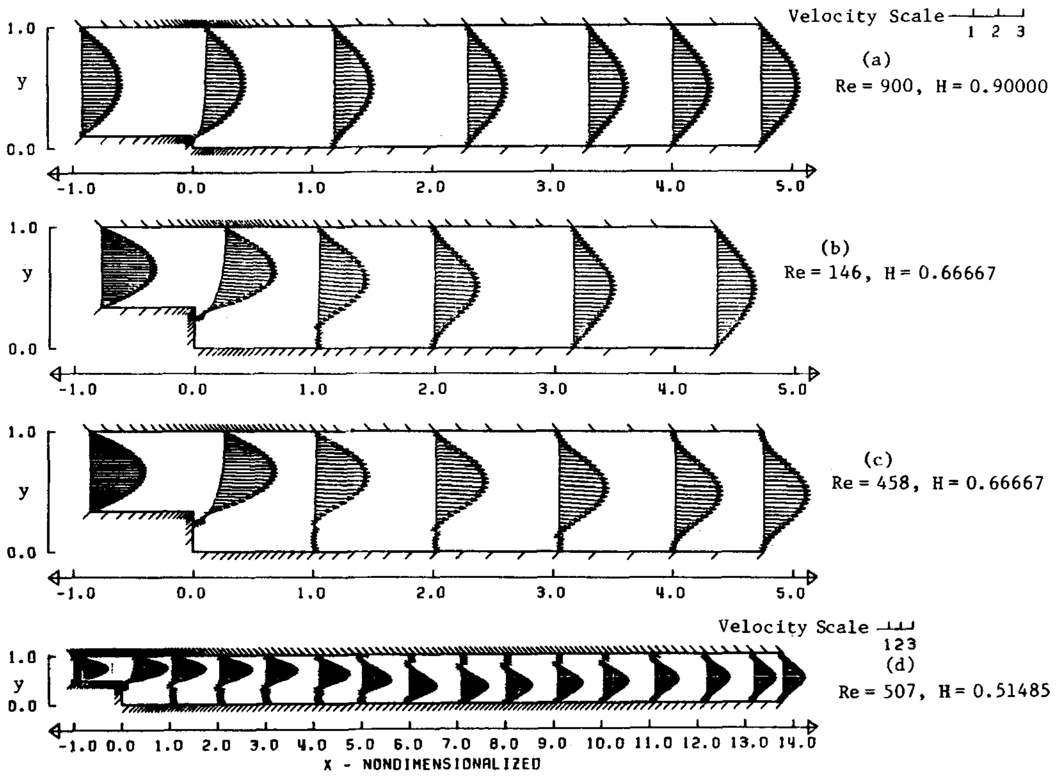

Figure 7. Steady state, total velocity vectors

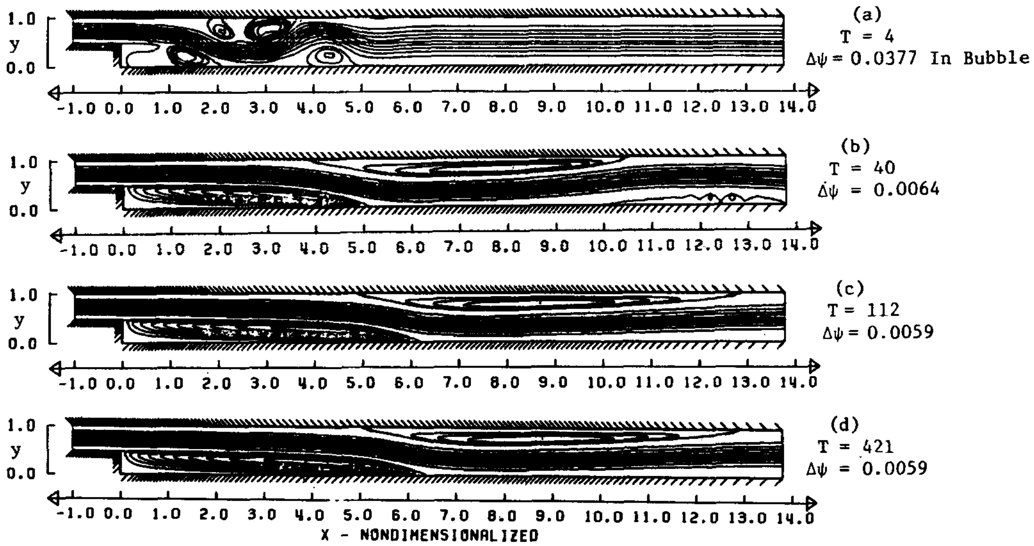

Figure 8. Transient streamfunction contours for $Re=600$; $\Delta\psi=0{\cdot}1$

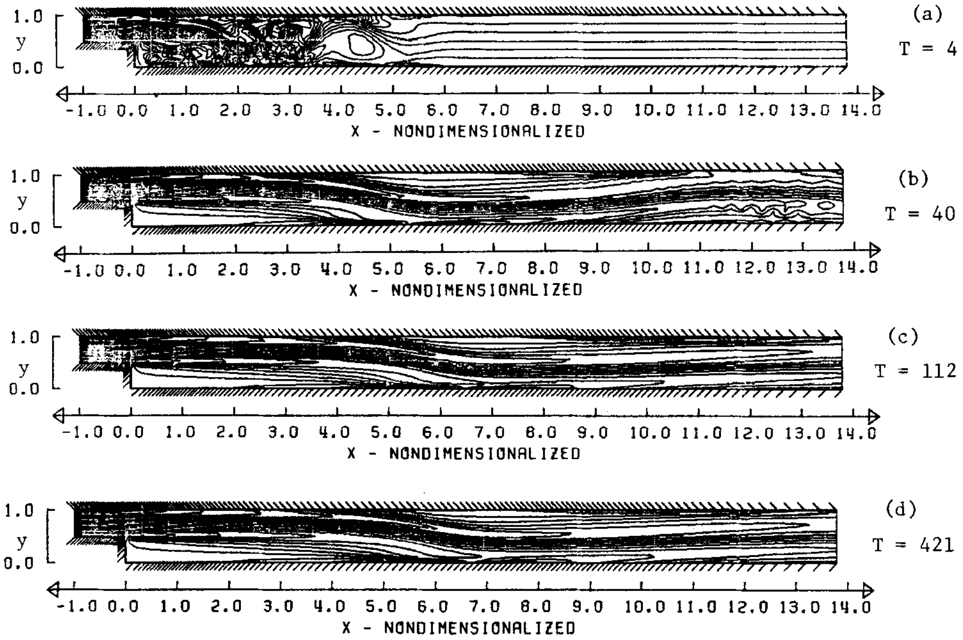

Figure 9. Transient vorticity contours for $Re = 600$; $\Delta\omega = 2{\cdot}0$

By the time $t = 40$ well developed primary, secondary and tertiary separation bubbles have been established along the upper and lower channel walls respectively, while the region of high disturbance has convected beyond $x \approx 20$. The remnants of the vortex street structure have been convected far downstream and are rapidly diminishing in intensity. By the time $t = 112$ the flow field has nearly achieved steady state, with well defined primary and secondary separation bubbles established along the channel walls downstream of the backward facing step. These separation bubbles continue to gradually diminish in intensity as they elongate in the downstream direction, until at $t = 421$ the steady state criterion of equation (32) is met and no further change is observed in the flow structure. At $t = 421$ the maximum absolute change occurs in the vorticity field near the outflow boundary, with the streamfunction and the near-step region of the flow having stabilized much earlier. Finally, the transverse profiles of the total velocity vector, along ξ^2 lines, at selected streamwise locations, are shown in Figure 10. Two regions of strong reversed flow are observed both on the lower and the upper walls.

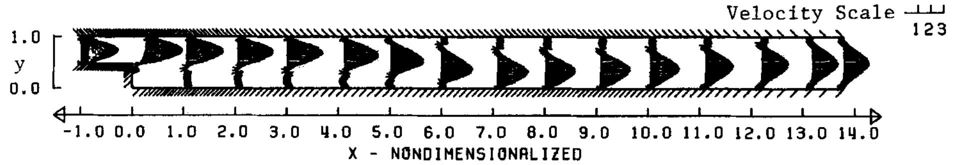

Figure 10. Steady state, total velocity vectors for $Re = 600$

6. CONCLUSIONS

An analysis has been developed, using the unsteady Navier–Stokes equations in generalized curvilinear co-ordinates, to study 2D incompressible separated flows. The discretized problem is formulated using central differences for the spatial derivatives, thus avoiding artificial viscosity. The ADI method has been used to solve the transport equation, whereas the BGE method is used to solve the Dirichlet Poisson problem. The overall accuracy of the numerical solution is $O[\Delta t, (\Delta\xi^1)^2, (\Delta\xi^2)^2]$.

The numerical method developed is applied to the separated flow inside a backstep channel. The results of the present analysis are verified extensively by comparison with the available experimental data for Re_S ranging from 72 to 565. For the configurations with only one separation bubble at the lower wall, there exists a similarity with respect to the backstep channel geometry. Hence the reattachment length L_1/h_s of the primary separation bubble on the lower wall, for various geometries, collapses into a single curve when plotted versus Re_S. On the other hand, the configurations with an additional separation bubble at the upper wall show a marked change in the reattachment length L_1 of the lower wall separation bubble. To the authors' knowledge, similar results have not been previously reported in the literature.

The unsteady analysis provides an accurate and efficient determination of the transient flow in the backstep channel. The shedding of vortices at the corner of the step, the formation of additional separation bubbles at the lower wall and the occurrence of the upper wall separation bubble are observed in the present results, which provide the detailed time-dependent structure for this flow. The analysis of this separated flow in the transitional regime of *Re* appears feasible with this unsteady analysis. Osswald *et al.*[37] have employed these efficient direct inversion techniques to solve the three-dimensional unsteady incompressible Navier–Stokes equations using a velocity–vorticity ($\mathbf{V}$, $\boldsymbol{\omega}$) formulation. This three-dimensional work is fully second-order-accurate in both time and space. Efforts to upgrade the temporal accuracy of the present 2D method to second order are currently underway. Also, the Reynolds stresses are being evaluated, from first principles, using the complete knowledge of the instantaneous motion as well as the mean motion. Ghoniem and Sethian[38] have provided turbulence statistics for these flows using their random vortex method.

REFERENCES

1. R. T. Davis and M. J. Werle, 'Progress on interacting boundary-layer computations at high Reynolds number', *Proc. First Symp. on Numerical and Physical Aspects of Aerodynamic Flows,* Long Beach, CA, 1981.
2. K. Stewartson, 'Multistructured boundary layers on flat plates and related bodies', *Advances in Applied Mechanics,* Vol. 14, Academic Press, 1974, pp. 145–239.
3. V. V. Sychev, 'On laminar separation', *Mehanika Zhidkosti i Gaza,* **3,** 47–59 (1972).
4. A. F. Messiter, 'Laminar separation: a local asymptotic flow description for constant pressure downstream', in *Flow Separation, AGARD Conf. Proc. on Flow Separation, CP 168,* 1975.
5. F. T. Smith, 'The laminar separation of an incompressible fluid streaming past a smooth surface', *Proc. Roy. Soc. A,* **356,** 443 (1977).
6. F. T. Smith, 'Laminar flow of an incompressible fluid streaming past a bluff body, the separation, reattachment, eddy properties and drag', *J. Fluid Mech.,* **92,** Part 1, 171–205 (1979).
7. J. Steger, 'Implicit finite-difference simulation of flow about arbitrary two-dimensional geometries', *AIAA J.,* **16,** 679–686 (1978).
8. S. G. Rubin, 'Incompressible Navier–Stokes and parabolized Navier–Stokes solution procedures and computational techniques', *VKI Lecture Notes for Series on Computational Fluid Dynamics,* 1982.
9. U. Ghia, K. N. Ghia, S. G. Rubin and P. K. Khosla, 'Study of separated flow in a channel using primitive variables', *Comput. Fluids,* **9,** 123–142 (1981).
10. K. N. Ghia and U. Ghia, 'Semi-elliptic globally-iterative analysis for two-dimensional subsonic internal viscous flows', presented at *NASA–Lewis Workshop on Computational Fluid Mechanics,* Cleveland, OH, 20–21 October 1982.
11. W. R. Briley, 'A numerical study of laminar separation bubbles using the Navier–Stokes equations', *J. Fluid Mech.,* **47,** Part 4, 713–736 (1971).

12. U. Ghia and R. T. Davis, 'Navier–Stokes solutions for flow past a class of two-dimensional semi-infinite bodies', *AIAA J.*, **12**, 1659–1665 (1974).
13. H. McDonald, S. J. Shamroth and W. R. Briley, 'Transonic flows with viscous effects', in R. E. Meyer (ed.), *Transonic, Shock and Multi-Dimensional Flows: Advances in Scientific Computing*, Academic Press, 1982.
14. G. A. Osswald and K. Ghia, 'Study of unsteady incompressible flow using nonuniform curvilinear grids, time marching and a direct method', *Multigrid Methods, NASA CP-2202*, October 1981.
15. K. Stuben, 'On the construction of fast solvers for elliptic equations', *VKI Lecture Notes*, Brussels, 29 March–2 April, 1982.
16. B. L. Buzbee, G. H. Golub and C. W. Nielson, 'On direct methods for solving Poisson's equations', *SIAM J. Numer. Anal.*, **7**, 627–657 (1970).
17. F. W. Dorr, 'The direct solution of the discrete Poisson equation on a rectangle', *SIAM Rev.*, **12**, 248–263 (1970).
18. R. A. Sweet, 'Direct methods for the solution of Poisson's equation on a staggered grid', *J. Comput. Phys.*, **12**, 422–428 (1973).
19. R. A. Sweet, 'A direct method for the discrete solution of separable elliptic equations', *SIAM J. Numer. Anal.*, **11**, 506–520 (1974).
20. U. Schumann and R. A. Sweet, 'A direct method for the solution of Poisson's equation with Neumann boundary conditions on a staggered grid of arbitrary size', *J. Comput. Phys.*, **20**, 171–182 (1976).
21. P. N. Schwarztrauber, 'A direct method for the discrete solution of separable elliptic equations', *SIAM J. Numer. Anal.*, **11**, 1136–1150 (1974).
22. M. K. Denham, and M. A. Patrick, 'Laminar flow over a downstream-facing step in a two-dimensional flow channel', *Trans. Inst. Chem. Eng.*, **52**, 361–367 (1974).
23. B. F. Armaly and F. Durst, 'Reattachment length and circulation regions downstream of a two-dimensional single backward facing step', *Momentum and Heat Transfer Processes in Recirculating Flows, HTD-Vol. 13*, ASME, New York, 1980, pp. 1–8.
24. P. J. Roache and T. J. Mueller, 'Numerical solutions of laminar separated flows', *AIAA J.*, **8**, 530–538 (1970).
25. A. D. Gosman and W. M. Pun, 'Lecture notes for course entitled: Calculation of recirculating flow', *Heat Transfer Report HTS/74/2*, Imperial College, London, 1973.
26. G. A. Osswald, 'A direct numerical method for the solution of unsteady Navier–Stokes equations in generalized orthogonal coordinates', *Ph.D. Dissertation*, University of Cincinnati, Cincinnati, OH, 1983.
27. K. N. Ghia, W. L. Hankey and J. K. Hodge, 'Study of incompressible Navier–Stokes equations in primitive variables using implicit numerical technique', *AIAA Paper No. 77-648*, 1977; also *AIAA J.*, **17**, 298–301 (1979).
28. A. Kumar and K. Yajnik, 'Internal separated flows at large Reynolds number', *J. Fluid Mech.*, **97**, Part 1, 27–51 (1980).
29. R. M. Beam and R. F. Warming, 'Implicit numerical methods for the compressible Navier–Stokes and Euler equations', *VKI Lecture Notes*, Brussels, 29 March–2 April, 1982.
30. B. F. Armaly, F. Durst, J. C. F. Pereira and B. Schönung, 'Experimental and theoretical investigation of backward-facing step flow', *J. Fluid Mech.*, **127**, 473–496 (1983).
31. A. M. O. Smith, 'On the growth of Taylor–Görtler vortices along highly concave walls', *Q. Appl. Math.*, **13**, 233–262 (1955).
32. G. R. Inger, 'Generation of streamwise vortices in separating nominally two-dimensional boundary layer flow', *18th Midwestern Mechanics Conf.*, University of Iowa, 1983, pp. 193–196.
33. S. G. Rubin and P. K. Khosla, 'Navier–Stokes calculations with a coupled strongly implicit method—I, Finite difference solutions', *Comput. Fluids*, **9**, 163–180 (1981).
34. K. N. Ghia, G. A. Osswald and U. Ghia, 'A direct method for the solution of unsteady two-dimensional incompressible Navier–Stokes equations', *Proc. Second Symp. on Numerical and Physical Aspects of Aerodynamic Flows*, Long Beach, CA, 1983.
35. G. A. Osswald, K. N. Ghia and U. Ghia, 'Steady of incompressible separated flow using an implicit time-dependent technique', *AIAA-CP 834*, 1983, pp. 686–696.
36. J. Kim and P. Moin, 'Application of a fractional-step method to incompressible Navier–Stokes equations', *J. Comput. Phys.*, **59**, 308–323 (1985).
37. G. A. Osswald, K. N. Ghia and U. Ghia, 'A direct algorithm for solution of incompressible three-dimensional unsteady Navier–Stokes equations', *AIAA CP-874*, 1987, pp. 408–421.
38. A. G. Ghoniem and J. A. Sethian, 'Effect of Reynolds number on the structure of recirculating flow', *AIAA J.*, **25**, 168–171 (1987).